Karhunen, J.; Lomanowski, B.; Solokha, V.; Aleiferis, S.; Carvalho, P.; Groth, M.; Kumpulainen, H.; Lawson, K. D.; Meigs, A. G.; Shaw, A.; JET Contributors

Estimation of 2D distributions of electron density and temperature in the JET divertor from tomographic reconstructions of deuterium Balmer line emission

Published in:
Nuclear Materials and Energy

DOI:
10.1016/j.nme.2020.100831

Published: 01/12/2020

Document Version
Publisher's PDF, also known as Version of record

Nuclear Materials and Energy 25 (2020) 100831

Contents lists available at ScienceDirect

Nuclear Materials and Energy

journal homepage: www.elsevier.com/locate/nme

Estimation of 2D distributions of electron density and temperature in the JET divertor from tomographic reconstructions of deuterium Balmer line emission

J. Karhunen [a,*], B. Lomanowski [b], V. Solokha [a], S. Aleiferis [c], P. Carvalho [d], M. Groth [a], H. Kumpulainen [a], K.D. Lawson [e], A.G. Meigs [e], A. Shaw [e], JET Contributors[1]

[a] Aalto University, Department of Applied Physics, 02150 Espoo, Finland
[b] Oak Ridge National Laboratory, Oak Ridge, TN 37831, USA
[c] Institute of Nuclear and Radiological Sciences and Technology, Energy and Safety, National Center for Scientific Research 'Demokritos', Athens 15310, Greece
[d] Instituto de Plasmas e Fusão Nuclear, Instituto Superior Técnico, 1049-001 Lisboa, Portugal
[e] CCFE, Culham Science Centre, Abingdon OX14 3DB, UK

ARTICLE INFO

Keywords:
Fusion
Detachment
Divertor physics
Divertor spectroscopy
Camera tomography

ABSTRACT

Estimates for 2D distributions of electron density, n_e, and temperature, T_e, have been obtained using reflection-corrected tomographic reconstructions of deuterium Balmer line emission in the JET divertor. The solutions are obtained by a two-dimensional Monte Carlo optimization model, based on intensity ratios of the Balmer D_α, D_γ and D_ε emission and the ADAS photon emission coefficients with additional constraints provided by line-integrated spectroscopic measurements of n_e and T_e. Synthetic benchmarks utilizing EDGE2D-EIRENE simulation outputs yield reproduction of reference n_e and T_e distributions within 25% with statistical error estimates of 5–15%. Experimental analysis of an L-mode n_e ramp shows extension and movement of the outer divertor high-n_e region with $n_{e,div}$ up to 1.5×10^{20} m^{-3} from the outer strike point to above the X-point and decrease of the divertor T_e to the range of 0.5–1.0 eV within 25% agreement with the line-integrated measurements. Comparison between the local estimates and their corresponding line integrals suggests underestimation of n_e and T_e by up to 75% and 50%, respectively, due to the geometric effects of line integration.

1. Introduction

Measurements of the electron density, n_e, and temperature, T_e, in the divertor volume are critical parameters in constraining divertor plasma simulations for interpretation of the plasma conditions and the volumetric physical phenomena leading to detachment. In JET, where the divertor is spectroscopically covered by a set of vertical lines-of-sight [1,2], divertor n_e and T_e are routinely resolved from Stark broadening of high-excitation Balmer lines of deuterium [3,4] and the spectral shape of the continuum emission [5,6], respectively. However, due to their line-integrated nature, the localization of the aforementioned measurements is limited to 1D profiles, providing emission-weighed averages while leaving the spatial details of the n_e and T_e distributions unsolved, if the emission is observed across a large volume.

Implications on the 2D characteristics of the JET divertor plasma can be made with the help of tomographic reconstructions of images from the tangential spectroscopic divertor camera system (KL11) [7–10], equipped with a selection of narrow bandpass filters for visible-range emission of the deuterium Balmer lines and various impurity species. The relative increase of recombination-dominated Balmer lines intensities in the divertor has previously been used for indirect identification of recombining low-temperature regions in JET [9,11,12], as well as several other tokamaks, such as Alcator C-Mod [5,13,14], DIII-D [15], ASDEX Upgrade [16] and JT-60U [17]. More recently, a sophisticated Bayesian method for resolving the divertor plasma conditions by simultaneous synthetization of measurements from multiple divertor diagnostics, including camera observations of the deuterium Balmer lines, has been developed for MAST Upgrade [18]. However, direct inference of the n_e and T_e distributions in the JET divertor has not been performed before.

* Corresponding author.
E-mail address: juuso.karhunen@aalto.fi (J. Karhunen).
[1] See the author list of E. Joffrin et al., Nuclear Fusion 59 (2019) 112021.

https://doi.org/10.1016/j.nme.2020.100831
Received 31 July 2020; Received in revised form 25 September 2020; Accepted 28 October 2020
Available online 4 November 2020

In this work, a Monte Carlo optimization tool has been developed for estimating the 2D distributions of n_e and T_e in the JET divertor based on simultaneous investigation of tomographic reconstructions of three different deuterium Balmer lines and atomic data from the ADAS [19] database. An additional constraint is obtained by coupling the method to the line-integrated n_e and T_e measurements. The 2D estimates have been benchmarked with the help of EDGE2D-EIRENE [20–22] simulations and performed for a JET ITER-like wall L-mode density ramp pulse for experimental assessment of the evolution of the n_e and T_e distributions during the course of detachment of the outer divertor.

2. Solving 2D n_e and T_e distributions from Balmer line ratios

2.1. Monte Carlo optimization of n_e and T_e with help of ADAS data

The emission intensity of a given atomic spectral line, such as the deuterium Balmer lines, can be described by the collisional-radiative model as a sum of light emitted in collisional excitation of neutral atoms and radiative recombination of singly ionized ions according to

$$I_{p\to q} = \left[n_0 n_e PEC_{p\to q}(n_e,T_e)^{exc} + n_i n_e PEC_{p\to q}(n_e,T_e)^{rec}\right]/4\pi. \quad (1)$$

Here, the electronic transmission is between the upper and lower energy states with respective principal quantum numbers p and q, n_0 and n_i are the densities of deuterium atoms and ions, respectively, and the photon emission coefficients, $PEC_{p\to q}(n_e,T_e)^{exc/rec}$, given by the ADAS database, describe the n_e and T_e dependence of the population of the emitting excited states due to excitation and recombination processes.

The estimation of the 2D n_e and T_e distributions relies on 2D emission distributions obtained by tomographic reconstructions of filtered divertor camera images of deuterium Balmer lines. The reconstructions are generated by methods presented in [10], utilizing consideration of reflections from the metallic wall surfaces – whose principle is thoroughly described in [23] and effects on the reconstructions discussed in [10,24] – and a recently introduced alignment correction between the camera image and the applied geometry calibration [25]. Balancing the number of unknown variables in equation (1), the current divertor camera set-up of JET allows simultaneous measurement of three different deuterium Balmer lines: D_α (p = 3 → q = 2, 656.1 nm), D_γ (p = 5 → q = 2, 433.9 nm) and either D_β (p = 4 → q = 2, 486.0 nm) or D_ε (p = 7 → q = 2, 396.9 nm). For this analysis, D_ε is chosen over D_β due to its high excitation state, which makes the D_ε emission strongly dominated by recombination and provides thus more distinct n_e and T_e behaviour of the PECs than D_β with respect to the PECs of the D_α and D_γ lines.

Solving the neutral density, n_0, with the help of equation (1) and the assumption of $n_i \approx n_e$ separately from the I_α/I_ε and I_γ/I_ε intensity ratios and equating the solutions yields

$$\begin{aligned}&\left(PEC_\gamma^{exc}PEC_\varepsilon^{rec} - PEC_\gamma^{rec}PEC_\varepsilon^{exc}\right)I_\alpha/I_\varepsilon - \left(PEC_\alpha^{exc}PEC_\alpha^{rec}\right.\\ &\left. - PEC_\alpha^{rec}PEC_\varepsilon^{exc}\right)I_\gamma/I_\varepsilon + PEC_\alpha^{exc}PEC_\gamma^{rec} - PEC_\alpha^{rec}PEC_\gamma^{exc}\\ &= 0, \end{aligned} \quad (2)$$

where a notational simplification of $PEC(n_e,T_e) \to PEC$ is made for clarity. Due to the substitution of $n_i \approx n_e$, the plasma is assumed to be reasonably pure. In the event of a notable increase of the effective charge state, Z_{eff}, of the divertor plasma due to, e.g., impurity seeding, this assumption needs to be re-assessed by considering the impurity concentrations in the divertor plasma. With I_α, I_γ and I_ε being given by measurements, the remaining unknowns in equation (2) are n_e and T_e through the implicit dependencies of the PECs, making equation (2) a non-analytic optimization problem of two variables. The solution is sought individually in each cell of the tomography grid by a Markov chain Monte Carlo (MCMC) [26,27] optimization model which also provides statistical error estimates for n_e and T_e. While the fundamental principle of inferring the divertor conditions by Monte Carlo optimization bears a resemblance to the Bayesian multi-diagnostics approach described in [18], the method presented here is less complex and built around a fixed set of diagnostics. Moreover, unlike in [18], the optimization is performed individually cell-by-cell instead of treating the plasma parameters as 2D fields.

Knowledge on n_e and T_e enables also estimation of atomic deuterium density from the intensities of the low-excitation-state D_α and D_γ lines, for which the excitation component in equation (1) is noticeable, as well as further analysis of the ionization and recombination distributions. The initial analysis of the neutral conditions and ionization and recombination rates in the divertor has provided physically reasonable results in qualitative agreement with predictions from EDGE2D-EIRENE modelling. These aspects will be reported elsewhere, while this work focuses on the n_e and T_e distributions only.

2.2. Constraining the optimization with line-integrated n_e and T_e measurements

The MCMC optimization is coupled to line-integrated spectroscopic measurements of the divertor n_e and T_e, based on Stark broadening of the D_δ line [4] and the spectral shape of the continuum emission [5,6], respectively, providing additional constraint to equation (2) in the optimization process. The 2D solutions of n_e and T_e of the MCMC model are initially obtained by allowing n_e and T_e to range uniformly within 0.01–5.0 × 10^{21} m^{-3} and 0.5–30 eV, respectively, in the optimization. The solutions are used to synthesize the line-integrated measurements utilizing the parameterization of the Stark broadening of the D_ε line presented in [4] and the ADAS functionalities for continuum emission [13]. The initial 2D solutions are scaled based on comparison between the experimental and synthesized line-integrated n_e and T_e measurements, and the updated distributions are used as initial values for a second round of MCMC optimization. The constraint is introduced on this round by allowing n_e and T_e in each cell to range within 50% of the corresponding initial value, given by the aforementioned scaling. Typically, a single correction round is sufficient to yield a closer correspondence between the experimental and synthesized line-integrated measurements than the allowed ±50-% variation, but the correction round can be repeated multiple times to improve the correspondence, if required. The results in this work have been obtained with a single correction round.

The effect of reflections from the metallic wall surfaces on the line-integrated spectroscopic n_e and T_e measurements is not addressed in the constraint of the MCMC model. Reflections re-distribute spectral features arising from local n_e and T_e conditions in the brightest emission regions to other areas in the divertor, where they blend into the observed signal. This can affect the values of n_e and T_e inferred from the spectral shape in regions where the contribution of the reflections from the bright emission regions is comparable to the locally observed emission. Earlier modelling work [6,10,28] has shown this to be the case especially for T_e measurements in which reflections of the strong continuum emission from the low-temperature regions have been observed to decrease the values inferred elsewhere in the divertor by 20–50% and by up to 75% in the most remote regions. However, in high-density detached divertor conditions, such as the ones studied in this work, the effect has been found to be less prominent due to the majority of the spectroscopic lines-of-sight propagating through the widened emission region, reducing the relative contribution of reflections in the observed signal. Unwanted bias in constraining the MCMC model due to the possible effect of reflections on the line-integrated n_e and T_e measurements is thus believed to be avoided by assuming that the effect is less significant than the ±50-% variation range allowed in the constraint.

2.3. Potential effects of molecular emission and Lyman emission opacity

Due to the restrictions of the ADAS collisional-radiative model, the effect of molecules is not considered in the analysis. However, earlier

experiments and modelling work [29–32] suggest that molecular processes can play a noticeable role in excitation of deuterium atoms, leading to Balmer line emission and enhancing especially the D_α intensity. Given the lesser effect on the D_γ and D_ε intensities and the line-integrated constraints set on n_e and T_e, the predominant effect of the presence of molecules is hypothesized to be possible overestimation of the inferred neutral density due to this emission being interpreted as increased excitation component of D_α. However, an additional impact on the n_e and T_e estimates cannot be ruled out either. Resolving the significance of the molecular contribution to the Balmer line emission and addressing its effect on the inference of the divertor conditions requires further investigation utilizing both divertor plasma modelling and experimental analysis, such as the methodology presented in [32], and is not attempted as part of the work presented here.

In addition to the omission of molecules, Lyman emission opacity of the divertor is not considered. While the plasma can be assumed to be optically thin for the Balmer lines [33], the populations of the excitation levels are affected by strong re-absorption of the Lyman ($p \rightarrow 1$) line emission, leading to increase in the Balmer emission intensities with respect to the standard optically thin ADAS PECs [6,34]. The contribution of Lyman opacity in the validity of solving n_e and T_e from equation (2) requires dedicated assessment in more detail, whereas here it is assumed that its effect on the analysis is attenuated by the consideration of ratios rather than absolute values of the intensities.

3. Benchmarks with synthetic emission

The MCMC optimization tool was tested with synthetic emission distributions calculated from solutions of an EDGE2D-EIRENE density scan. The simulations describe divertor conditions before and after the onset of outer divertor detachment in L mode. This provides a variety of emission characteristics with reference distributions of n_e and T_e available for comparison with the estimates given by the MCMC model.

Without added noise in the emission distributions, the MCMC model reproduces the $n_{e,div}$ and $T_{e,div}$ distributions within 10% of the respective references, as shown in Fig. 1, with statistical error estimates of 5–15%. Simultaneously, the emission intensities of D_α, D_γ and D_ε are reproduced with an accuracy of approximately 5%. The performance indicates that tool is not excessively prone to local minima or weak parametric dependencies of the line ratios in the (n_e,T_e) space.

To mimic degraded signal-to-noise ratio in actual measurements, noise was introduced in the synthetic emission distributions at levels between 5 and 50% of the peak emission intensities. Without additional constraints to equation (2), this lead to a significant reduction in the accuracy of the MCMC estimates for both $n_{e,div}$ and $T_{e,div}$ with the results ranging within 75% of the references at the highest noise levels. This is visualized by the wide scattering of the blue data points in Fig. 1. However, coupling the MCMC model to line-integrated inference of $n_{e,div}$ and $T_{e,div}$, as discussed in Section 2.2, retains the reproductability of the reference $n_{e,div}$ and $T_{e,div}$ distributions within 25%. This indicates the added robustness due to the coupling and its vital role in the capability of providing tolerable estimates also when the quality of the camera data is compromised.

4. Evolution of divertor n_e and T_e distributions during outer divertor detachment in L mode

4.1. Balmer line emission distributions in different states of outer divertor detachment

Analysis of the 2D $n_{e,div}$ and $T_{e,div}$ distributions was performed for the L-mode density ramp pulse 94759 with plasma current and toroidal magnetic field of I_p = -2.45 MA and B_ϕ = 2.45 T and Ohmic and neutral beam heating powers of P_{Ohm} = 1.6–2.2 MW and P_{NBI} = 1.0 MW. The line-integrated edge density at the outer midplane, given by interferometry, ranged within $n_{e,edge,LFS} = 2.5–5.1 \times 10^{19}$ m^{-3}. The plasma was

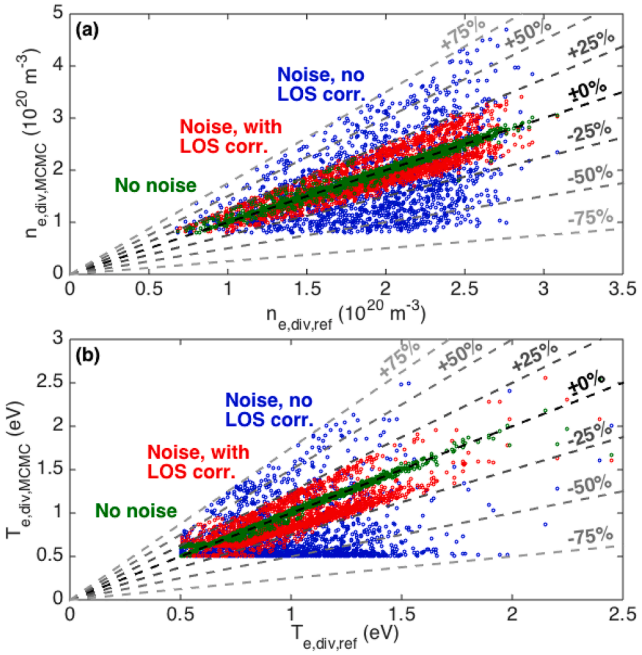

Fig. 1. The MCMC optimization model reproduces the reference $n_{e,div}$ (a) and $T_{e,div}$ (b) distributions, provided by EDGE2D-EIRENE simulations, within accuracy of 10% in the absence of noise (green). Introduction of noise reduces the accuracy of the reproduction to within 75% of the references (blue) for both $n_{e,div}$ and $T_{e,div}$, while coupling to the line-integrated spectroscopic $n_{e,div}$ and $T_{e,div}$ measurements retains the correspondence within 25% even in the presence of noise (red). The black dashed lines indicate exact reproduction of the reference distributions ($n/T_{e,div,MCMC} = n/T_{e,div,ref}$), and the grey dashed lines correspond to over- and underestimation of the reference values by 25%, 50% and 75%. For clarity, the 5–15-% error bars are omitted from the figure.

unseeded with low effective charge state of Z_{eff} = 1.1–1.2. During the pulse, the roll-over of the total ion current at the outer target, indicating the onset of the particle detachment, took place almost immediately after the beginning of the n_e ramp at $n_{e,edge,LFS} \approx 2.8 \times 10^{19}$ m^{-3}, followed by deepening detachment with increasing upstream $n_{e,edge,LFS}$, as shown in Fig. 3a. Consequently, the results presented in this work represent different degrees of outer divertor detachment.

At the roll-over point of the outer target ion current, the emission of all studied Balmer lines is concentrated in the vicinity of the strike point in Fig. 2a, e and i. Qualitative deviations between low- and high-excitation lines are observed, as the emission distributions extend from the strike point to and above the X-point with proceeding detachment. The recombination-dominated D_ε distributions in Fig. 2j and k show more pronounced elongation between the strike point and the X-point than the D_α distributions in Fig. 2b and c, which peak more strongly at the strike point. This is attributed to the more prominent excitation component, proportional to the neutral density in equation (1), as well as the amplification of the D_α emission due to molecular processes, as discussed in Section 2.3. The differences between the D_α and D_ε patterns are most notable near the end of the n_e ramp, when the brightest D_ε emission is observed above the X-point in Fig. 2l, whereas the D_α peak remains in front of the outer target in Fig. 2d. With its emission characteristics lying between those of D_α and D_ε, the D_γ distributions in Fig. 2e–h show close qualitative resemblance to the D_ε distributions with more emphasis on the strike-point region in deep detachment due to the more pronounced excitation component.

4.2. Evolution of outer divertor n_e and T_e during detachment

The evolution of the emission patterns in Fig. 2 coincides with the shift of the high-n_e region in the outer divertor from the strike point to

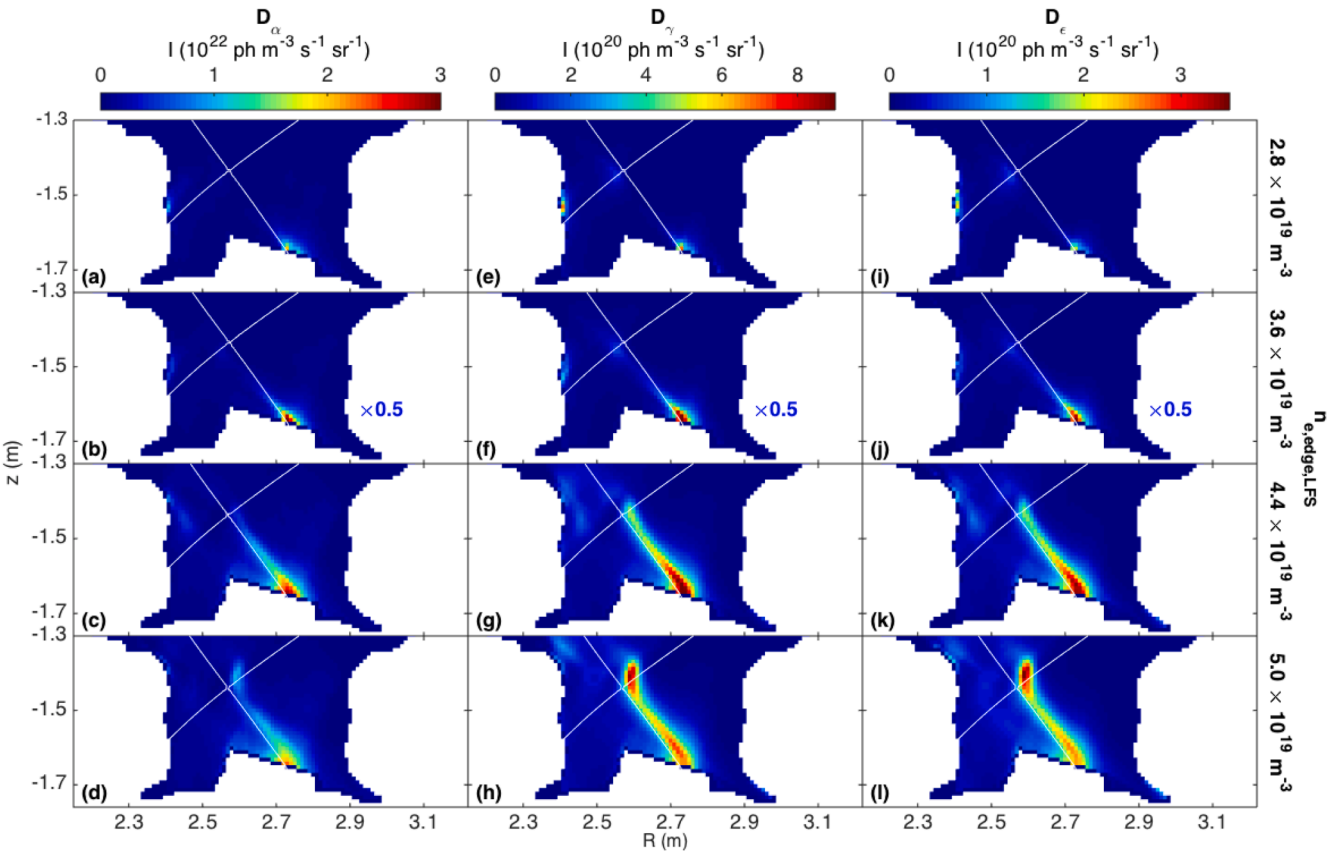

Fig. 2. Tomographic reconstructions of the Balmer D_α (a–d), D_γ (e–h) and D_ε (i–l) emission show extension of the emission distributions from the outer strike point to above the X-point with increasing degree of the outer divertor detachment at upstream densities of 2.8×10^{19} m^{-3} (a, e, i), 3.6×10^{19} m^{-3} (b, f, j), 4.4×10^{19} m^{-3} (c, g, k) and 5.0×10^{19} m^{-3} (d, h, l). The intensities in (b, f, j) have been scaled by a factor of 0.5 to improve the comparability of the qualitative characteristics of the emission distributions between the different upstream densities.

above the X-point, as indicated by the MCMC estimates in Fig. 3d–g. Simultaneously, the $T_{e,div}$ estimates in Fig. 3h–k decrease to 0.5–2.0 eV throughout the divertor.

At the outer strike point, the estimated electron temperature in Fig. 3c falls rapidly from 3–4 eV to approximately 1.5 eV in the beginning of the n_e ramp, as the outer target ion current rolls over at $n_{e,edge,LFS} \approx 2.8 \times 10^{19}$ m^{-3}, coinciding with steady increase of the estimated outer strike point electron density in Fig. 3b. At $n_{e,edge,LFS} \approx 3.2 \times 10^{19}$ m^{-3}, approximately 15% above the roll-over upstream n_e, the estimated $T_{e,div,OSP}$ has decreased to the order of 1 eV, and the strike-point density reaches its maximum value of $n_{e,div,OSP} \approx 8.0 \times 10^{20}$ m^{-3}. Until its peak, the density estimate agrees within error bars with Langmuir probe measurements of n_e at the outer strike point in Fig. 3b. Since the inference of n_e from the probe data suffers from unreliability of the probe analysis for T_e in the low temperature range of the experiment, the representativity of the n_e measurement was improved by using the T_e values derived from line-integrated divertor spectroscopy instead, as described in [6]. With deepening detachment, the camera data in Fig. 3b and c suggest decrease of $n_{e,div,OSP}$ to approximately 30% of its peak value and $T_{e,div,OSP}$ to 0.5–0.7 eV, reaching the low end of the T_e range set for the PECs in the optimization. For $n_{e,div,OSP}$, the Langmuir probe data shows significantly steeper decrease with increasing upstream n_e than the estimates inferred from the camera analysis. The deviation can partially be attributed to the unaccounted increase in the emission due to molecular processes near the outer target in detached conditions, the uncertainties of the camera analysis, such as remaining overestimation of the near-surface emission due to insufficient removal of reflection-induced artefacts in the tomography process, as well as the uncertainties of correcting the Langmuir probe measurements with T_e from line-integrated spectroscopy due to the widened emission volume at high densities [6]. It is also speculated that the emission-based measurements describe the plasma volume above the divertor target plate, where the decrease in $n_{e,div}$ during detachment may not be as significant as at the target surface, where the Langmuir probe measurements are carried out.

Halfway between the outer strike point and the X-point, at z = -1.53 m, Fig. 3b shows only a subtle increase in the divertor n_e to $n_{e,div} \approx 5.0 \times 10^{20}$ m^{-3}, as the high-n_e region spreads upwards from the outer strike point with increasing $n_{e,edge,LFS}$. The estimated $T_{e,div}$ at the same vertical level remains at approximately 1.0 eV, showing a slightly decreasing trend with increasing upstream n_e in Fig. 3c. The strongest increase in $n_{e,div}$ is observed immediately above the X-point, where Fig. 3b shows a steep increase to above $n_{e,div,X\text{-}p} = 1.5 \times 10^{21}$ m^{-3} at the end of the n_e ramp, when the outer divertor is in deep detachment. This coincides with a steep decrease in the X-point T_e from 3–4 eV to approximately 1.5 eV.

To provide a sufficient signal-to-noise ratio for the $n_{e,div}$ and $T_{e,div}$ analysis, the studied interval of the density ramp was selected by visual inspection such that the maximum intensity of the D_ε emission was clearly distinguishable from the background emission – in this case resulting in a lower D_ε intensity limit of the order of 10^{18} ph m^{-3}s^{-1}sr^{-1}. Furthermore, the analysis was spatially restricted to regions where the intensity of the D_ε emission is higher than 15% of the maximum D_ε intensity in each frame. At lower intensities, the emission becomes difficult to distinguish from noise and remaining background halos in the tomographic reconstructions. This inherently limits the spatial coverage of the emission-based 2D analysis, making it dependent on the divertor conditions. Consequently, the method does not provide similar wide mapping of the divertor as, e.g., obtained with the divertor Thomson scattering system of DIII-D [35–37] during plasma sweeps.

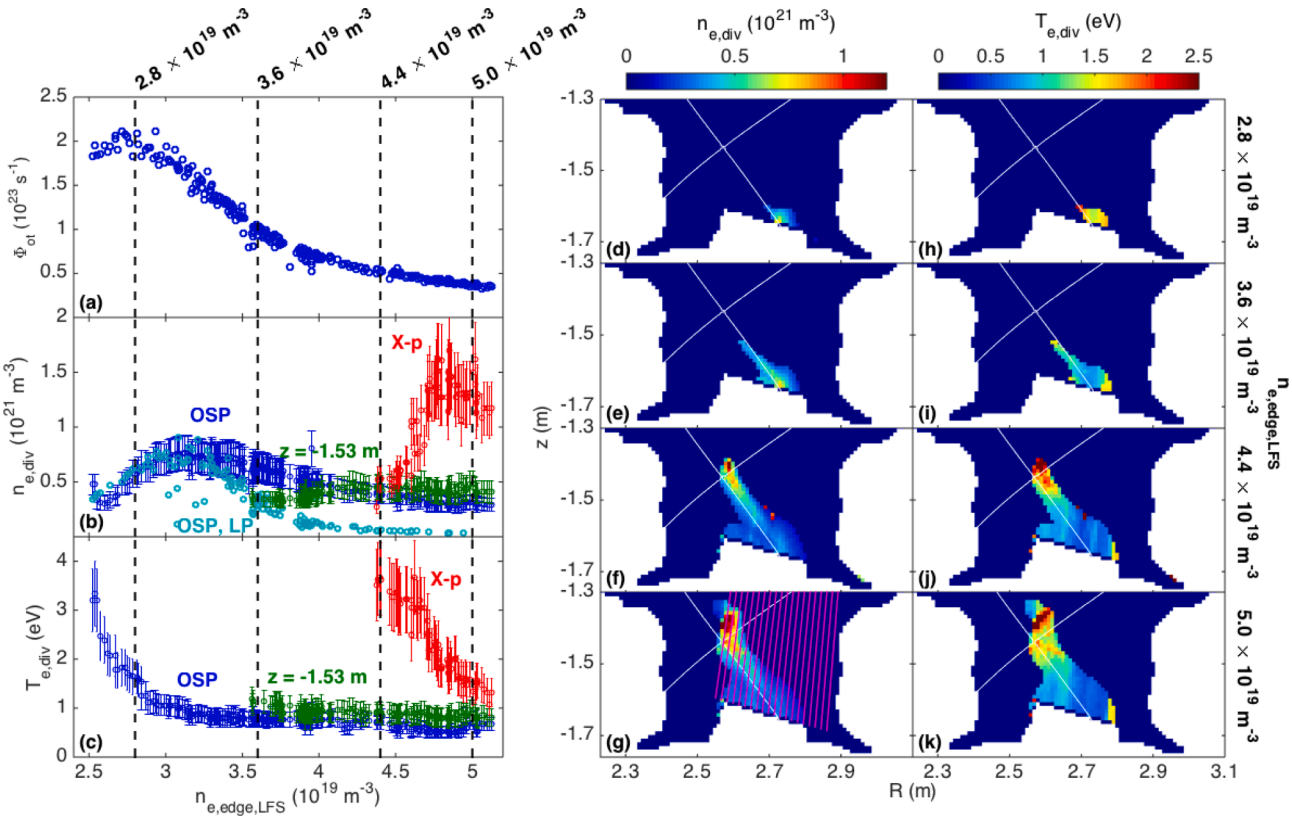

Fig. 3. Detachment of the outer divertor during the n_e ramp is indicated by roll-over and decay of the total ion current at the outer divertor target (a). The estimated 2D $n_{e,div}$ distributions (d–g) and local values (b) show peaking of $n_{e,div}$ at the outer strike point (OSP, blue) after the onset of detachment in agreement with the Langmuir probe data (LP, cyan), as well as steep increase of $n_{e,div}$ above the X-point (X-p, red) at the highest $n_{e,edge,LFS}$ and only subtle increase halfway between the aforementioned locations (z = -1.53 m, green). The 2D $T_{e,div}$ estimates (h–k) and the local values (c) suggest decrease of $T_{e,div}$ from 3–4 eV to 0.5 eV at the outer strike point and to 1.0–1.5 eV above the X-point with almost constant temperature at around 1.0 eV halfway between the outer strike point and the X-point. The vertical black dashed lines in (a–c) indicate the upstream densities presented in (d–k). The spectroscopic lines-of-sight used for line-integrated analysis are visualized with magenta lines in (g).

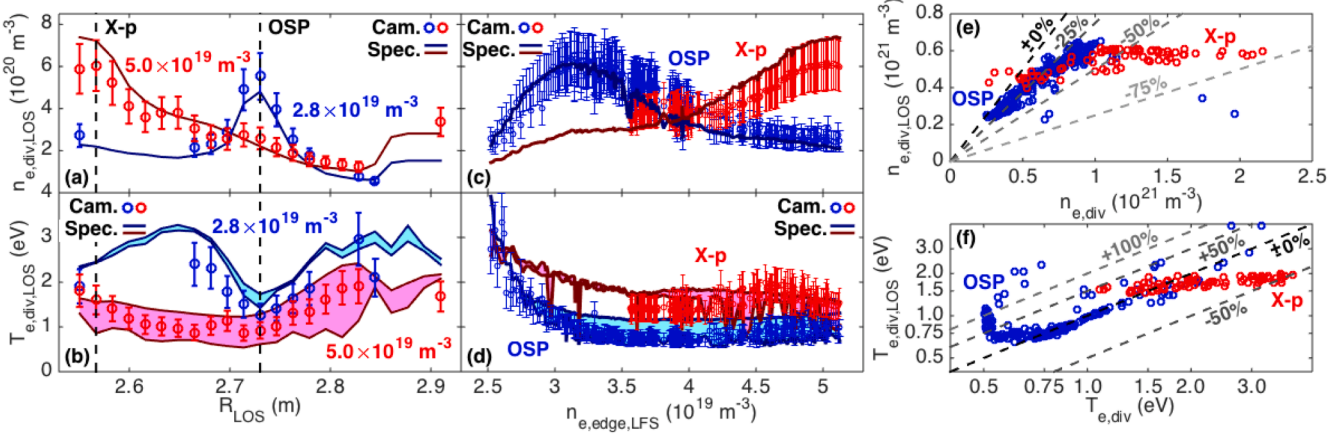

Fig. 4. Example radial profiles of line-integrated $n_{e,div}$ (a) and $T_{e,div}$ (b) at the onset of detachment (blue) and in deep detachment (red) show agreement primarily within 20% between the spectroscopic measurements and synthetically derived line integrals of the 2D estimates. Similar agreement is observed throughout the n_e ramp for both $n_{e,div}$ (c) and $T_{e,div}$ (d) at the outer strike point (blue) and above the X-point (red). The solid lines in (a–d) correspond to the spectroscopic measurements (Spec.), whereas the line integrals of the 2D estimates inferred from the camera analysis (Cam.) are plotted with data points. The shaded regions in (b, d) cover the bracket between the upper and lower limits of the T_e measurements. The line-integrated measurements underestimate $n_{e,div}$ (e) by 25–40% at the outer strike point (blue) and by up to 75% at the X-point (red). For $T_{e,div}$ (f), the line integral provides a good representation of the local $T_{e,div}$ at the outer strike point (blue) with the exception of the $T_{e,div} \approx 0.5$ eV range, while underestimation by up to 50% is observed at the X-point (red). The black dashed lines indicate similarity between the line-integrated and local values ($n/T_{e,div,LOS} = n/T_{e,div}$) in both (e) and (f), and the grey dashed lines correspond to underestimation of the local $n_{e,div}$ by 25%, 50% and 75% in (e) and under- and/or overestimation of the local $T_{e,div}$ by 50% and 100% in (f). Note the logarithmic axes in (f).

4.3. Comparison to line-integrated spectroscopic measurements

As discussed in Section 3, the coupling between the 2D camera estimates and line-integrated spectroscopic measurements of $n_{e,div}$ and $T_{e,div}$ provides an effective constraint for the former method, enabling improved consistency between the camera analysis and the established measurements of the divertor conditions. Symbiotically, the expansion of the analysis to 2D allows investigation of the effect of line integration on the spectroscopic measurements, improving the spatial precision of the divertor measurements.

The line-integrated n_e values, inferred synthetically from the 2D estimates, indicate primarily agreement within 20% with the spectroscopic measurements in Fig. 4a and c, showcasing the effectiveness of constraining the initial values of the MCMC optimization. However, Fig. 4c suggests that the MCMC estimates tend to systematically underestimate the line-integrated X-point density at high upstream n_e, when the density peak shifts to the X-point region, while the agreement still remains within error bars. Also the synthetic line-integrated $T_{e,div}$ measurements in Fig. 4b and d mostly fall between the upper and lower limits of the spectroscopic measurements, given by the fits in different wavelength regions of the continuum spectrum, as described in [6]. In the case of the synthetic $T_{e,div}$ measurements, the data presented in Fig. 4 corresponds to the average of these upper and lower limits which were observed to yield a significantly narrower range than for the actual spectroscopic measurements. This is likely due to the spatial restrictions of the MCMC estimates leading to integration through a smaller variety of plasma conditions than in real spectroscopic measurements. It is noted that while the spectroscopic n_e and T_e measurements are inherently affected by reflections from wall surfaces, taking this into account for the synthetic measurements was not possible in this work without more advanced forward modelling of the synthetic spectroscopy with the help of ray-tracing. However, as discussed in Section 2.2, the effect of reflections is not expected to be significant in the studied high-density detached conditions and should thus not interfere with the comparability between the data in Fig. 4a–d.

Comparison between the local estimate of $n_{e,div}$ at the outer strike point and the line-integrated values inferred synthetically from the 2D estimates along the spectroscopic line-of-sight observing the outer strike point in Fig. 4e suggests that the line integration underestimates the local value by approximately 40% after the roll-over, when $n_{e,div,OSP}$ is at its highest. When the high-n_e region moves away from the strike point, the underestimation is narrowed to 25%. Similar trend was observed also by post-processing EDGE2D-EIRENE simulations in [6], albeit the investigation did not extend as deep into detachment as in this work. At the X-point, more drastic differences are observed, as the underestimation steadily increases to 75% of the local $n_{e,div}$ above the X-point. The significant mismatch can be explained by the vertically elongated shapes of the D_ε emission and $n_{e,div}$ distributions above the X-point in deep detachment, leading to the corresponding spectroscopic line-of-sight integrating emission through a variety of different densities. At the outer strike point, the emission and $n_{e,div}$ are more narrowly distributed with respect to the line-of-sight geometry, providing a more local description of $n_{e,div}$ than at the X-point.

For $T_{e,div}$, Fig. 4f indicates that the line-integrated measurement provides a good representation of the local value at the outer strike point with the exception of the lowest values of $T_{e,div,OSP} \approx 0.5$ eV which the line-integrated measurements overestimate by up to a factor of 2. The increasingly significant overestimation at the lowest strike-point temperatures follows the observations made in [6] and is attributed to widening of the continuum emission distribution and the outer strike point becoming colder in deep detachment than other regions observed by the same spectroscopic line-of-sight. At the X-point, the line-integrated $T_{e,div}$ measurements suffer from the same geometric effect as the line-integrated $n_{e,div}$ measurements, and the local $T_{e,div}$ values are underestimated by up to 50%.

5. Conclusions

A Monte Carlo optimization model was adapted for estimating 2D distributions of the electron density and temperature in the JET divertor based on tomographic reconstructions of filtered divertor camera images of different deuterium Balmer emission lines with the help of the ADAS collisional-radiative model. For added constraint and robustness, the method is coupled to the established line-integrated spectroscopic measurements of the divertor n_e and T_e. Benchmarks with synthetic emission data from EDGE2D-EIRENE simulations show agreement within 10–25% between the $n_{e,div}$ and $T_{e,div}$ distributions derived from the Balmer emission and the reference distributions from the simulation outputs. The estimates are provided with statistical error bars of 5–15%.

Estimates of the outer divertor n_e during a JET L-mode density ramp pulse show extension and shift of the high-n_e region from the outer strike point to above the X-point, as the outer divertor proceeds from the onset of detachment to deep detachment. At the outer strike point, the estimated density peaks at $n_{e,div} \approx 8.0 \times 10^{20}$ m^{-3} slightly after the onset of detachment, while a steep increase to $n_{e,div} \approx 1.5 \times 10^{21}$ m^{-3} is observed above the X-point in deep detachment near the end of the n_e ramp. Simultaneously, the estimated $T_{e,div}$ decreases from 3–4 eV to approximately 0.5 eV at the outer strike point and 1.5 eV above the X-point with deepening detachment.

Replicating the line-integrated spectroscopic $n_{e,div}$ and $T_{e,div}$ measurements synthetically with the 2D estimates shows agreement within 20% with the actual spectroscopic measurements, indicating effective coupling between the two diagnostics in the analysis. Comparisons between the local estimates and the line-integrated estimates along corresponding lines-of-sight suggest that the line integration underestimates $n_{e,div}$ at the outer strike point by 25–40%, whereas underestimation of up to 75% is observed at the X-point due to the longer integration path of the line-of-sight through different density regions. The line-integrated $T_{e,div}$ measurements were found to represent the local values at the outer strike point accurately with the exception of the lowest estimated local temperatures at approximately 0.5 eV which are overestimated by up to a factor of two. Similarly to the $n_{e,div}$ measurements, the geometry of the spectroscopic lines-of-sight with respect to the emission and $T_{e,div}$ distributions leads to the line-integrated measurements underestimating the X-point temperature by up to 50%.

The ability to estimate the radial and poloidal extent of the divertor n_e and T_e distributions improves the local comparability between experiments and divertor modelling by avoiding the spatial averaging of line-integrated measurements. The knowledge of local $n_{e,div}$ and $T_{e,div}$ also allows analysis of the neutral conditions, as well as the ionization and recombination characteristics of the divertor plasma, as will be reported elsewhere. However, further investigations are still required to assess the representativity of the estimates, when also the contribution of molecular processes to the Balmer line emission and the effect of the Lyman emission opacity on the validity of the ADAS photon emission coefficients of the Balmer lines is considered.

CRediT authorship contribution statement

J. Karhunen: Conceptualization, Methodology, Software, Formal analysis, Investigation, Writing - original draft, Visualization. **B. Lomanowski:** Conceptualization, Formal analysis. **V. Solokha:** Methodology, Software. **S. Aleiferis:** Investigation. **P. Carvalho:** Investigation. **M. Groth:** Investigation, Supervision. **H. Kumpulainen:** Investigation. **K.D. Lawson:** Investigation. **A.G. Meigs:** Investigation. **A. Shaw:** Investigation. **:** .

Declaration of Competing Interest

The authors declare that they have no known competing financial interests or personal relationships that could have appeared to influence the work reported in this paper.

Acknowledgements

This work has been carried out within the framework of the EUROfusion Consortium and has received funding from the Euratom research and training programme 2014-2018 and 2019-2020 under grant agreement No 633053. The views and opinions expressed herein do not necessarily reflect those of the European Commission.

References

[1] A.G. Meigs, et al., Rev. Sci. Instrum. 81 (2010) 10E532.
[2] B. Lomanowski, et al., Rev. Sci. Instrum. 85 (2014) 11E432.
[3] A.G. Meigs et al., 27th EPS Conference on Plasma Physics (2000) 1264–1267.
[4] B. Lomanowski, et al., Nucl. Fusion 55 (2015), 123028.
[5] D. Lumma, et al., Phys. Plasmas 4 (1997) 2555.
[6] B. Lomanowski, et al., Plasma Phys. Controlled Fusion 62 (2020), 065006.
[7] A. Huber, et al., Rev. Sci. Instrum. 83 (2012) 10D511.
[8] J. Harrison, et al., J. Nucl. Mater. 415 (2011) S379–S382.
[9] A. Huber, et al., J. Nucl. Mater. 438 (2013) S139–S147.
[10] J. Karhunen, et al., Rev. Sci. Instrum. 90 (2019), 103504.
[11] A. Huber, et al., J. Nucl. Mater. 463 (2015) 445–449.
[12] A. Huber, et al., Nucl. Fusion 57 (2017), 086007.
[13] J.L. Terry, et al., Phys. Plasmas 5 (1998) 1759.
[14] B. Lipschultz, et al., Phys. Rev. Lett. 81 (1998) 1007–1010.
[15] R.C. Isler, et al., Phys. Plasmas 4 (1997) 2989.
[16] S. Potzel, et al., Nucl. Fusion 54 (2014), 013001.
[17] K. Fujimoto, et al., Plasma Fusion Res. 4 (2009) 025.
[18] C. Bowman, et al., Plasma Phys. Controlled Fusion 62 (2020), 045014.
[19] H.P. Summers, The ADAS User Manual, version 2.6 (2004), http://www.adas.ac.uk.
[20] R. Simonini, et al., Contrib. Plasma Phys. 34 (1997) 368.
[21] D. Reiter, et al., J. Nucl. Mater. 196–198 (1992) 80–89.
[22] S. Wiesen, "EDGE2D/EIRENE code interface report", JET ITC-Report (2006), www.eirene.de/e2deir_report_40jun06.pdf.
[23] M. Carr, et al., Rev. Sci. Instrum. 90 (2019), 043504.
[24] J. Karhunen, et al., J. Instrum. 14 (2019) C10013.
[25] S. Silburn, A. Meakins, T. Farley. (2019, November 6), euratom-software/calcam: Calcam v2.4 (Version v2.4.0), Zenodo, http://doi.org/10.5281/zenodo.3530201.
[26] W.K. Hastings, Biometrika 57 (1970) 97–109.
[27] A. Patil, et al., J. Stat. Softw. 35 (2010) 1–81.
[28] B. Lomanowski, et al., Nuclear Mater. Energy 20 (2019), 100676.
[29] M. Groth, et al., Nuclear Materials and Energy 19 (2019) 211–217.
[30] S. Menmuir, et al., J. Quant. Spectrosc. Radiat. Transfer 105 (2007) 425–437.
[31] R. Dey, et al., Nucl. Fusion 59 (2019), 076005.
[32] K. Verhaegh et al., Plasma Physics and Controlled Fusion (submitted).
[33] C.F. Maggi, et al., J. Nucl. Mater. 266–269 (1999) 867–872.
[34] K. Behringer, et al., New J. Phys. 2 (2000) 23.1—23.19.
[35] T.N. Carlstrom, et al., Rev. Sci. Instrum. 66 (1995) 493.
[36] F. Glass, et al., Rev. Sci. Instrum. 87 (2016) 11E508.
[37] T.N. Carlstrom, et al., Rev. Sci. Instrum. 89 (2018) 10C111.